

Development and characterization of the JNE concentrator

Shuai Ouyang^a, Yuzi Yang^b, Yang Zhang^a, Aiqiang Zhang^b, Haoyan Yang^c, Changxu Wei^b,
Yuhao Liu^d, Zhe Wang^b, Tao Xue^c, Zongyi Wang^d, Shaomin Chen^b

^aKey Laboratory of Particle Physics and Particle Irradiation (MOE), Institute of Frontier and Interdisciplinary Science, Shandong University, Qingdao, Shandong 266237, China

^bDepartment of Physics & Center for High Energy Physics, Tsinghua University, Beijing 100084, P.R. China

^cKey Laboratory of Particle & Radiation Imaging (Tsinghua University), Ministry of Education, Qinghuayuan Street No. 1, Beijing, China

^dSchool of Civil and Hydraulic Engineering, Huazhong University of Science and Technology, Wuhan 430074, China

Abstract. The Jinping Neutrino Experiment (JNE) will utilize approximately 3000 8-inch MCP-PMTs identified as GDB-6082 from North Night Vision Technology to detect neutrinos. To enhance the effective coverage of the JNE detector, mounting a custom-designed light concentrator on each photomultiplier tube (PMT) is a practical and economical approach. We measured angular responses of the concentration factor at four wavelengths in air medium for the concentrator with the selected cutoff angle of 70° . The measurements align with the Monte Carlo simulations. Furthermore, our results indicate that these concentrators can improve the efficiency of light collection by 40% under parallel illumination conditions. However, this enhancement results in a slight increase in transit-time spread, with the full width at half maximum (FWHM) increasing by less than 0.3 ns. We conclude that the developed light concentrators are highly suitable for the JNE.

Keywords: PMT, light concentrator, JNE, light collection efficiency.

*Yuzi Yang, yangyz18@tsinghua.org.cn *Yang Zhang, yangzhangsdu@email.sdu.edu.cn

Contents

1	Introduction	2
2	The design of the concentrator	3
2.1	The MCP-PMT of GDB-6082	4
2.2	Light bowl	4
2.3	Assembly structure	5
3	Material	8
3.1	Material	8
3.2	Reflecting surface	8
4	Validation of the concentration factor	9
4.1	The test facility	9
4.2	Data analysis	11
4.2.1	Waveform analysis	11
4.2.2	Concentration factor	12
4.3	Monte Carlo simulations	13
4.4	Systematic uncertainty	14
5	Discussion	14
5.1	Low background	14

5.2	The protection of aluminum film	14
5.3	Improvement of light collection efficiency and energy resolution	15

6 Conclusion 15

1 Introduction

The Jinping neutrino experiment (JNE)¹ is the next-generation solar neutrino experiment at the China Jinping Underground Laboratory (CJPL) with a rock overburden of approximately 2,400 meters.² As with other neutrino detectors,³⁻⁷ the JNE will install photomultiplier tubes (PMTs) to detect the photons emitted during particle interactions with matter and determine the particle's energy, position, and direction. Due to the extremely low probability of neutrinos interacting with matter, an ultralow background environment is essential to detect rare neutrino signals, including solar neutrinos,⁸ geoneutrinos,⁹ supernova neutrinos,¹⁰ and neutrinoless double beta decay.¹¹ The JNE is specifically being constructed to detect and study these neutrino signals.

The JNE detector (Fig. 1) consists of three layers: the innermost layer is a transparent acrylic sphere with a radius of 4.98 m, which is used to hold the target substance and allow light to pass through; the middle layer is an array of PMTs supported by a stainless steel frame, with a radius of 6.03 m, responsible for capturing the generated photons; the outermost layer is a water tank with dimensions of $14 \times 12.9 \times 13.2$ m, used to effectively shield the radioactive background in the external environment. The acrylic sphere is suspended within the detector using specially designed holding ropes to counteract gravitational or buoyancy forces.¹² This sphere can be filled with various target materials at different experimental stages, including pure water, the liquid scintillator,¹³ and the aqueous solution of LiCl.¹⁴

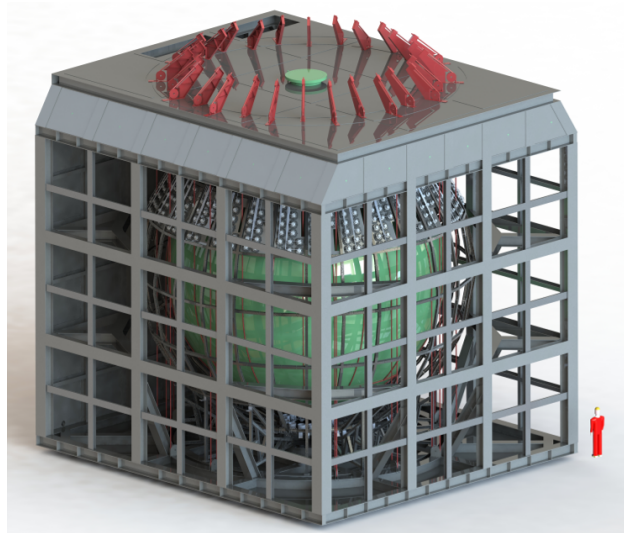


Fig 1 The key mechanical structure of the JNE detector, which mainly consists of three parts: the inner acrylic sphere, the PMTs and associated supporting grid in the middle, and the outermost water shield.

The micro-channel plate (MCP) PMTs identified as GDB-6082¹⁵ produced by North Night Vision Technology (NNVT) are selected as photon detection devices in the first place due to the high photon detection efficiency (DE) of up to 30%. Approximately 3000 MCP-PMTs will be deployed

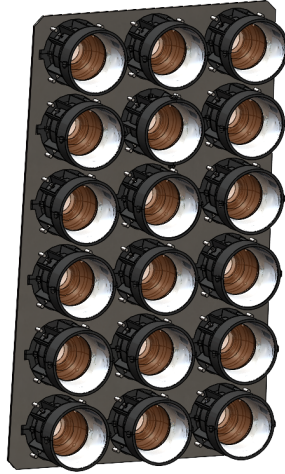


Fig 2 The combination of PMT plus concentrator as the photon detecting device.

in the JNE detector. The energy resolution of the JNE detector is closely related to its overall photon collection efficiency, which is improved by equipping the PMTs with light concentrators, as shown in Fig. 2. The PMTs, together with the concentrators, are installed on a stainless steel plate according to a modular and zoned configuration. Depending on the specific shapes of each zone, each module contains a varying number of PMTs. Eventually, each module is positioned on the corresponding PMT grid.

The application of light concentrators in neutrino experiments is effective in achieving excellent physics results, notably in the cases of SNO, SNO+, and Borexino.^{16–18} Furthermore, OSIRIS¹⁹ and KamLAND-Zen have also proposed incorporating concentrators into their detectors. In the realm of γ -ray astronomy, mounting light concentrators on SiPMs represents an additional viable strategy.^{20,21}

This paper describes the development and characterization of the concentrator. We have formulated a concentrator with a wide field of view and a high geometric collection efficiency based on mathematical and simulated studies.²² The concentrator functions by expanding the entrance aperture of the PMT and reflecting the incoming light onto the PMT's photocathode. As PMTs are expected to cover about 25% of the solid angle, a circular opening light concentrator is chosen to increase the effective coverage rather than a hexagonal one. On the other hand, the concentrator can shield light beyond the region of the cut-off angle, e.g., radioactivities from neighboring PMTs.

The structure of the article is as follows. Section 2 introduces the theoretical design scheme of the light concentrator; Section 3 discusses the selection of manufacturing materials and their mechanical performance; Section 4 elaborates on the validation of the concentration factor via the experiment and Monte Carlo (MC) simulations; Section 5 and 6 contain the discussion and conclusion.

2 The design of the concentrator

The design of the reflector surface of the concentrator takes into account the maximization of the light reflection efficiency and good contact with the photocathode, and the characteristics of the photocathode, such as DE and transit time spread (TTS), to ensure that the combination of PMT plus concentrator is in the optimal working condition. Although adding concentrators around the

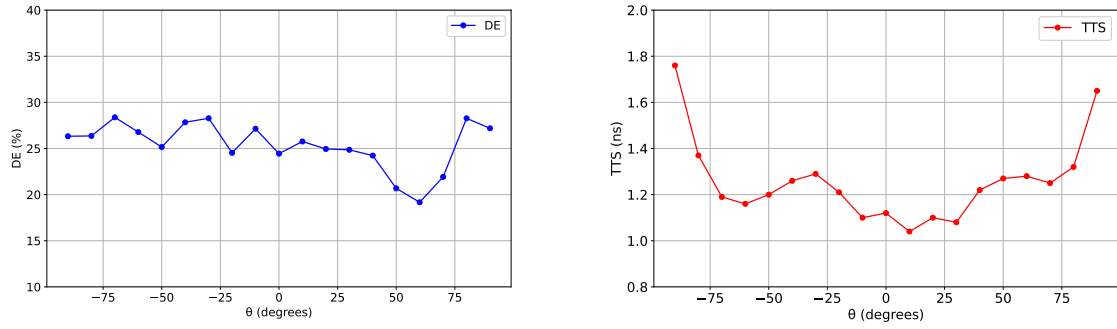


Fig 3 The variation of DE (left) and TTS (right) of MCP-PMT (GDB-6082) with respect to zenith angle θ . Here, $\theta=0^\circ$ corresponds to the front vertex of the PMT ellipsoid, while $\theta=\pm 90^\circ$ corresponds to the equator of the ellipsoid. A significant increase in the vicinity of the equator is observed for the TTS scanning.

PMTs increases the diameter of the entrance aperture, it reduces the observed field of view. Therefore, it is imperative to determine the effective detection volume of the experiment to ensure that it can fully cover the acrylic sphere. In addition, the economy and practicality of the concentrator are also essential features. When choosing a simple and cost-effective design, it is necessary to ensure the safety and stability of the overall structure and adopt a convenient installation method to shorten the construction period.

2.1 The MCP-PMT of GDB-6082

The MCP-PMT (GDB-6082) comprises a glass ellipsoid, a glass neck, and a plastic base. The three semi-axes of the ellipsoid are 10.15, 10.15, and 7.36 cm in length, with the photocathode distributed on the front part above the ellipsoid's equator. The ellipsoid has a highly reflective aluminum-coated layer below the equator and around the neck, which can effectively reflect incident light back to the photocathode. The base is made of ABS plastic and houses a voltage divider module and is filled with waterproof and oil-resistant materials. Generally, when the voltage is around 1700 V, the photoelectron gain of PMT can reach an order of magnitude of 10^7 .

The performance of PMT has been extensively studied in various aspects, including DE, TTS, dark count rates (DCR), the probability of pre-pulses and after-pulses, the single-electron response (SER) and a long tail in the charge distribution,¹⁵ which is parameterized with a physical model.²³ In addition, the TTS is unevenly distributed with respect to the zenith angle (θ) in the ellipsoid (see Fig. 3) and increases significantly near the equatorial plane of the ellipsoid, while the correlation between the DE and the elevation angle is relatively small. This indicates that the transit time of the photoelectrons emitting near the equator is longer, which leads to an increased TTS and affects the accurate measurement of a particle's energy-deposition position within the detector. We could mask this equatorial region using the light concentrator.

2.2 Light bowl

The light bowl used is designed based on a 3D-modified string method.²² In this method, the key parameters that determine the shape of the light bowl are the light exit aperture and the cutoff angle. Higher collection efficiency of photons requires a larger entry aperture of a light bowl, and thus a larger exit aperture. So, it is best to set the exit aperture of the light bowl to coincide with

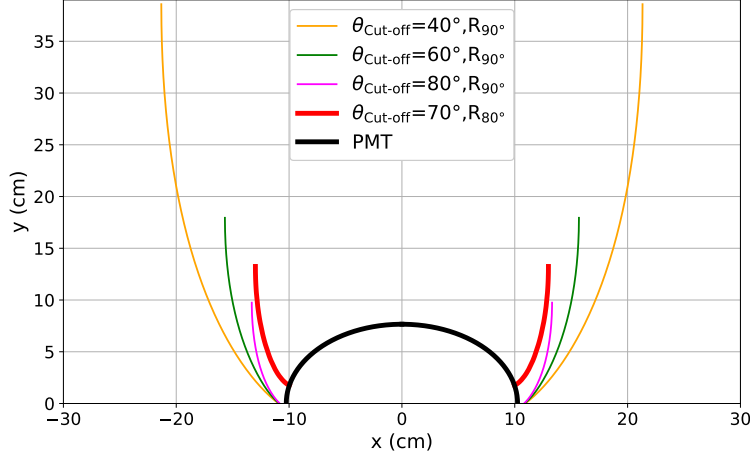


Fig 4 The cross-section of the PMT and concentrator with different cut-off angles $\theta_{\text{Cut-off}}$ in the xy plane. Here, R_{90° represents that its exit aperture is aligned with the equator of the PMT, while R_{80° indicates that its exit aperture is located at $\pm 80^\circ$.

the equatorial plane of the PMT photocathode. However, as shown in Fig. 3, for the MCP-PMT used in JNE, the TTS around the equatorial plane of the photocathode is quite high, leading to a poorer position resolution and discrimination between scintillation and Cherenkov light, which is essential for particle identification. As a result, only the part with a zenith angle less than $|\pm 80^\circ|$ of the photocathode is used, where a TTS less than 1.4 ns is guaranteed. The exit aperture of the light bowl is thus a circle with a radius of 9.98 cm and 1.76 cm higher than the equatorial plane of the photocathode. By this design, the PMT also benefits from being tightly clamped by the concentrator.

The modified string method ensures that most rays with an incident angle less than the cut-off angle reach the PMT photocathode either directly or after a few reflections. As illustrated in Fig. 4, a higher cut-off angle results in a lower and narrower light bowl, allowing more rays from a broader range to be collected. This leads to a larger effective detection volume, which can be calculated as detailed in Fig. 5.

In this context, light bowls of the concentrator with cut-off angles in the range $60^\circ - 70^\circ$ are compared based on several parameters: the radius of the effective detection volume (R_{eff}), the maximum allowed installation error (α), the ratio of the entrance aperture to the exit aperture area of the PMT (R_S), the average photon transition time (T_{tr}) defined as the mean time difference from passing through the entrance aperture to the photocathode, and T_{tts} , measured using the full width at half maximum. The α in Fig. 5 shows the maximum angular tolerance in which the effective detection volume just covers the liquid scintillator. Table 1 summarizes the results. Given that the angle error during PMT installation may reach a maximum of 10° , we have chosen the light bowl with the cut-off angle of 70° , as shown in Fig. 4.

2.3 Assembly structure

A specialized assembly system has been designed to properly secure the light bowl at the top of the PMT and to facilitate the installation of both the PMT and the light bowl on the grid shell of the JNE detector. The basic structure of the assembly scheme presented in this paper consists

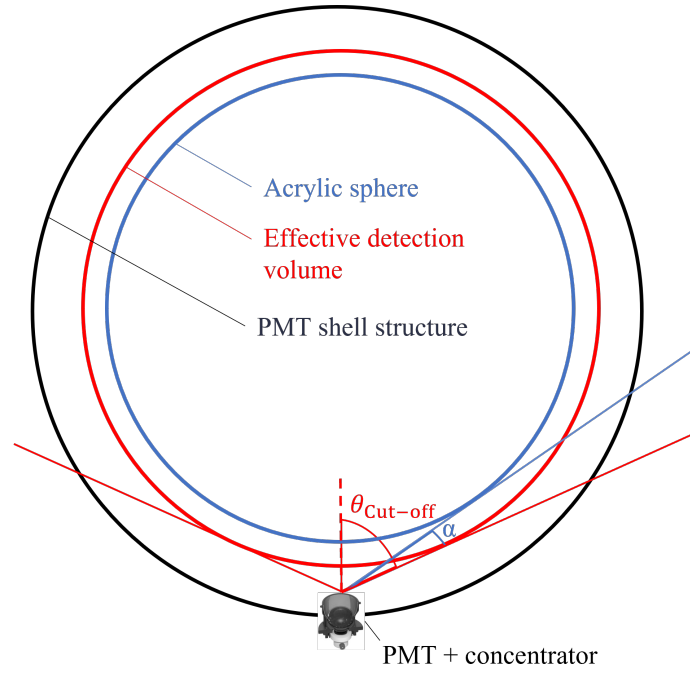


Fig 5 The cut-off angle $\theta_{\text{Cut-off}}$, installation error angle α and effective detector volume of a single PMT equipped with a concentrator. Within the error range, the acrylic spherical detector of JNE is completely contained within the effective detection volume.

Table 1 The key parameters of the different light bowls obtained through calculation and simulation include: the cut-off angle $\theta_{\text{Cut-off}}$, the radius of the effective detection volume R_{eff} , the maximum allowable installation error angle α , the ratio of the entrance aperture to the exit aperture area of the PMT R_S , and the transmission time T_{tt} and the total transmission time spread T_{tts} brought about by the use of the concentrator. During the calculation and simulation process, the exit aperture is fixed at $\theta = \pm 80^\circ$. When conducting the simulation analysis for T_{tt} and T_{tts} , the incident angle of the light is a random value ranging from 0 to $\theta_{\text{Cut-off}}$.

$\theta_{\text{Cut-off}} [^\circ]$	$R_{\text{eff}} [\text{m}]$	$\alpha [^\circ]$	R_S	Average $T_{tt} [\text{ns}]$	$T_{tts} [\text{ns}]$
70.0	5.43	10.22	1.60	0.47	0.27
69.0	5.39	9.15	1.63	0.49	0.23
68.0	5.35	8.08	1.66	0.50	0.27
67.0	5.32	7.00	1.68	0.52	0.23
66.0	5.27	5.92	1.71	0.53	0.23
65.0	5.23	4.84	1.74	0.55	0.27
64.0	5.19	3.76	1.77	0.57	0.23
63.0	5.14	2.67	1.81	0.59	0.23
62.0	5.09	1.57	1.84	0.60	0.23
61.0	5.04	0.48	1.88	0.63	0.20
60.0	4.99	0.31	1.92	0.65	0.23



Fig 6 The disassembly and assembly diagrams of MCP-PMT and concentrator. The structure of the concentrator mainly consisting of clamping cylinder, a light bowl, silicone rubber rings and clamping accessories.

primarily of a clamping cylinder, a light bowl, silicone rubber rings, and clamping accessories, as shown in Fig. 6.

The clamping cylinder features a symmetric design, ensuring a uniform force distribution on both sides. This design facilitates processing and production with the same set of molds. Furthermore, this structure can be directly connected to the detector cover plate using four M16 screws, allowing for a secure and quick installation.

The light bowl is a key working component of the light concentrator. Not only does it provide a reflective surface, but the curved structure at its bottom also ensures a close fit with the PMT, achieving stable fixation. During the design process, the shape tolerance of the PMT sphere was fully considered, achieving a seamless connection.

The silicone rubber ring, as the main clamping component of the light concentrator, is made of moderately hard silicone rubber material and is specially designed for the non-working area below the equator of the PMT sphere. The ring works in conjunction with the clamping cylinder and the light bowl to ensure secure clamping of the PMT head.

The clamping accessories include the fastening screws and nuts that assist in assembling and securing the overall structure.

3 Material

3.1 Material

In selecting the material for the light concentrator, we referred to research on the SNO experiment⁴ and the materials used in the PMT packaging structure,¹⁵ and ultimately chose high-performance ABS plastic.

ABS plastic offers several advantages: Its high strength allows it to support the weight of the PMT and its associated concentrator while withstanding the buoyancy the PMT experiences in water. Second, its excellent wear resistance and surface stress ensure that the shape of the light concentrator remains consistent over time. In addition, ABS plastic has stable chemical properties and is resistant to water and mineral oil, helping to prolong its service life. Finally, as a plastic material, its radioactive background can be well under control, thereby reducing interference to the signal of interest.

The mechanical properties of ABS plastic were measured using a uniaxial tensile test based on the guideline of ASTM D638-14.²⁴ The test recorded the stress-strain curve, which revealed the elastic modulus, tensile strength, and fracture behavior of the material. The results show that ABS has an average tensile strength of 37.14 MPa and an elastic modulus of 2392.92 MPa. The combined structure of PMT and the associated concentrator was modeled and sectioned into meshes using HyperMesh²⁵, and finite element analysis was performed with ABAQUS²⁶ to analyze the mechanics of the combined structure at four positions of different depths under water. The results are summarized in Table 2. The calculations show that the maximum principal stress is 0.60 MPa, which is about 1.6% of the tensile strength of ABS, demonstrating that ABS plastic is secure even at a 12-meter depth of water and is expected to remain stable for long-term operation.

Table 2 Summary of mechanical results of finite element analysis at four positions of different depths under water. The second column lists the depth of the position, and the third column shows the maximum principle stress.

Position	Depth (m)	Maximum principle stress (MPa)
A	1.77	0.56
B	6.03	0.40
C	10.29	0.49
D	12.03	0.60

3.2 Reflecting surface

Since aluminum has a strong reflectivity for light of different wavelengths, we selected it as the reflective layer of the light bowl. The reflectivity of aluminum in the visible light band (400-700 nm) can reach 80%, and it also maintains a high reflectivity in the ultraviolet region (part of the light-sensitive area of PMT¹⁵).

To achieve efficient reflective performance, we use vacuum coating technology to evenly coat aluminum on the light bowl made of ABS plastic and ensure that its thickness is greater than 50 nm. The surface roughness and oxidation can affect the reflectivity of the aluminum film. The reflectivity of coated aluminum versus wavelength and incident angle, as shown in Fig. 7 is measured using a UV/Vis/NIR spectrophotometer. Note that the reflectivity at 90° is not measured, but is assumed to be one as per the Fresnel law.

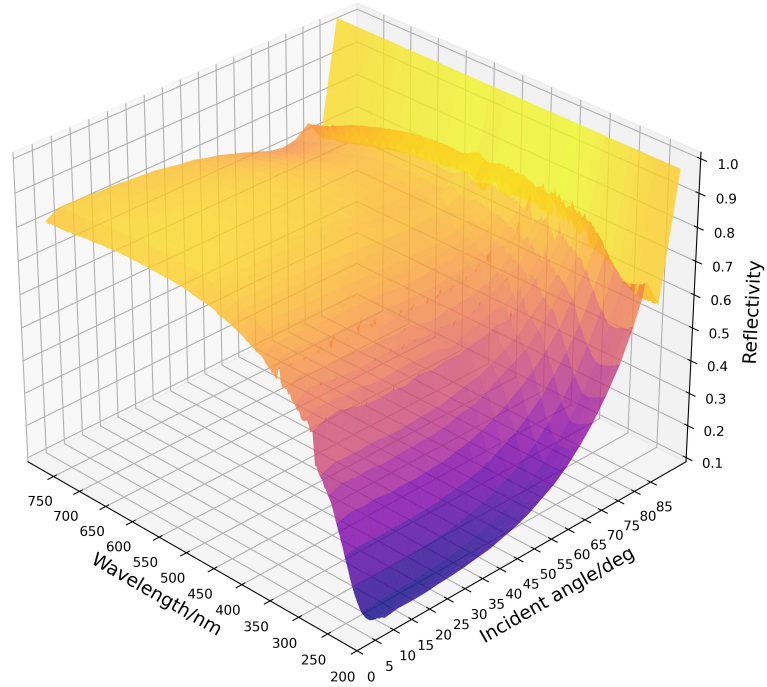


Fig 7 The reflectivity of the coated aluminum versus wavelength and incident angle.

4 Validation of the concentration factor

Through the collaborative efforts of the R&D team, we successfully fabricated the concentrator and completed its assembly with PMT. To assess the performance of the concentrator, we designed a dedicated test facility and conducted detailed experimental tests. We compared the experimental results with those obtained from Geant4 simulations. The consistency between the measured and simulated results demonstrated that the concentrator significantly enhanced the photon collection efficiency.

4.1 The test facility

As shown in Fig. 8, the device of the test facility mainly consists of four parts: a dark box, a light source system, a readout electronics system and a computer. This device is equipped with two PMTs, and the installation and removal operations of the concentrator can be conveniently carried out on one of the PMTs, thereby determining the concentrator's performance.

The black box is used to shield external light to ensure the accuracy of the experimental measurements. It measures $1.53 \times 1.43 \times 0.37$ m and is made of 1 cm thick black opaque acrylic plates. We frosted the inner sides of the acrylic plates to reduce the impact of internal light reflection on the test results. There are two sites to fix PMTs in the dark box: one is the calibration PMT, and the other is the test PMT. By obtaining the influence of the light bowl on the test tube, we determined the concentrator's performance. Two quarter-circular rails are installed at the bottom of the dark box, namely L1 and L2, allowing the light source to slide along the rails. These two rails share a common center, which is the center of the entrance aperture of the light bowl. The

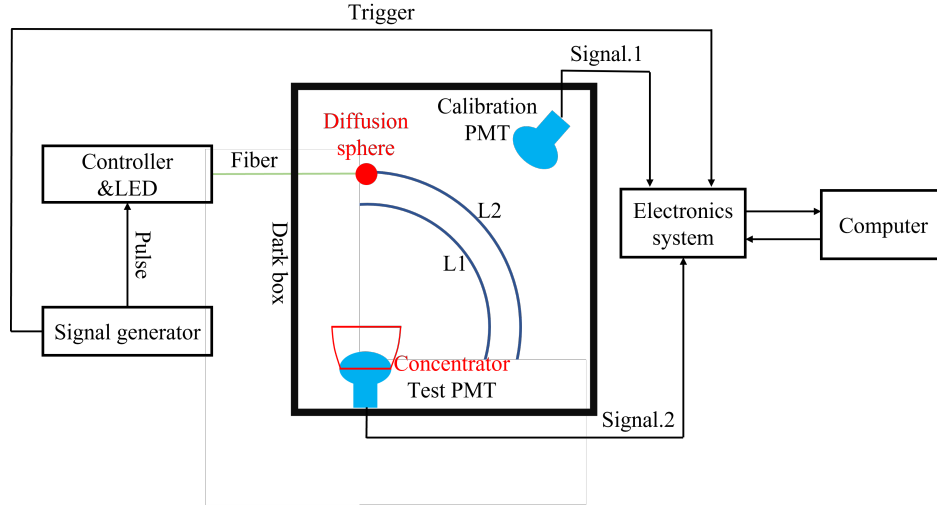


Fig 8 The test facility, including a dark box, a light source system, a readout electronics system and a computer.

radii of L1 and L2 are 50 and 75 cm, respectively. The stainless steel support columns on the rails ensure that the light source remains at the same horizontal level as the center of the light bowl.

The light source system consists of LEDs, a signal generator, a controller, a diffusion sphere, and an optical fiber. Its working principle is as follows: The signal generator generates pulse waveforms and outputs them to the controller. The controller then drives the LEDs to emit, transmitting through the optical fibers to the diffusion sphere inside the dark box for uniform emission. The LEDs in this system emit light at multiple monochromatic wavelengths, including 365, 415, 465, and 480 nm. The half-width of each wavelength is approximately 10 to 20 nm. We have configured the signal generator with different duty cycles to optimize the performance of LEDs at varying wavelengths. Specifically, the duty cycle for the 365 nm LED is set at about 3.5%, the duty cycles of the 465 nm and 480 nm LEDs are 2.0%, and the duty cycle of the 415 nm LED is only 0.2%. The pulse frequency generated by the signal generator is 100 kHz. The selected optical fibers are commercial-grade single-mode optical fibers, which can provide stable optical transmission performance. The diffusion sphere is made of polytetrafluoroethylene material and has a diameter of 5 cm.

The readout electronics system for this device was independently designed and manufactured by the R&D team. The waveform digitization board²⁷ comprises a system motherboard and an FPGA mezzanine card (FMC). The FMC utilizes the AD9695 from Analog Devices, which is a 1000 MSPS, 14-bit JESD204B ADC. It features two JESD204B channel outputs with a channel rate of up to 10 Gbps. Using DC input coupling, the input single-ended signal is converted to a differential signal through the fully differential amplifier LMH6654 from TI. The AD5686 from Analog Devices is used to bias the input signal to fully utilize the full-scale dynamic range of the AD9695, with a nominal value of 1.6 V. The motherboard of the system is a 6U CPCI standard module. It combines two FMC high pin count (HPC) connectors with an FPGA. Each FMC connector is connected to the FPGA through 58 LVDS signals and 8 pairs of high-speed serial transceiver signals. The theoretical bandwidth of each channel is 16.3 Gbps. The trigger input/output and the external reference clock input are designed on the front panel of the waveform digitizer board. A 64-bit DDR4 SDRAM is also designed to buffer real-time data. The self-developed ZYNQBee2 module based on Xilinx's ZYNQ7010 is used for slow control of digitizers

such as EPICS.

A computer is required to be equipped to control the electronic system, regulate the high voltage of the PMT, and collect and store data, in addition to the above equipments.

4.2 Data analysis

4.2.1 Waveform analysis

The left panel of Fig. 9 shows two typical waveforms of the calibration PMT and the test PMT. The waveforms were captured within a 1 us time window with a 1 GSPS sampling frequency. The baseline is subtracted to obtain the amplitude and time distributions of the photoelectron peaks. A prominent peak named pedestal is observed in the right panel of Fig.9, which can introduce significant noises, as shown in the left panel of Fig.10.

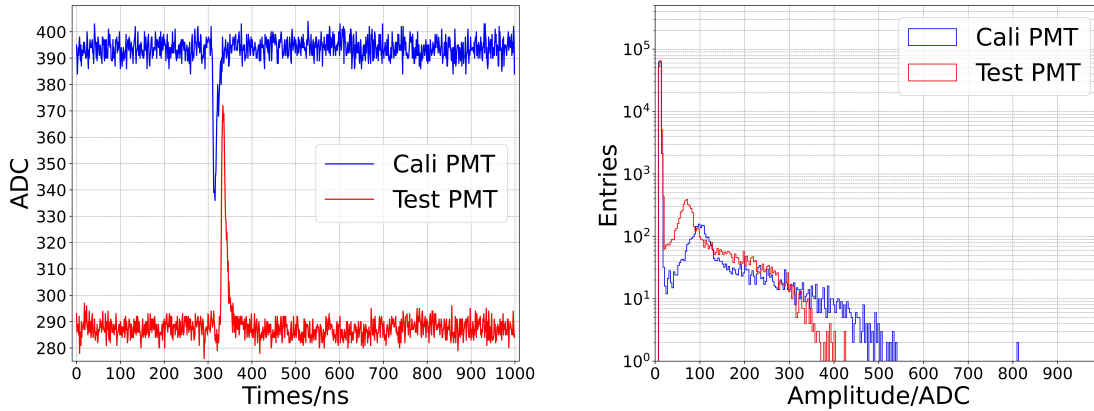


Fig 9 Left: two typical waveforms from the calibration PMT and the test PMT. Right: amplitude of photoelectron peaks from the calibration PMT and the test PMT. The blue (red) histogram corresponds to the calibration (test) PMT. Data shown as an example come from a certain run.

To eliminate the effect, we only select peaks whose amplitudes are greater than $\mu_{ped} + 5\sigma_{ped}$, where μ_{ped} and σ_{ped} are fitted from those amplitudes less than 30 ADC using a Gaussian. The signal loss due to this selection is assumed to be small since the peak-to-valley ratio of the amplitude distribution can be as large as about 7. After applying this selection, we have obtained the time distribution of the photoelectron peaks, as shown in the right panel of Fig. 10. A Gaussian function $G(t_{signal}, \sigma_{signal})$ is used to fit and determine the signal window $[t_{signal} - 3\sigma_{signal}, t_{signal} + 3\sigma_{signal}]$, from which the number of non-zero hits is counted. The contribution of dark noise hits is then subtracted based on estimations derived from the flat sideband beyond the signal window.

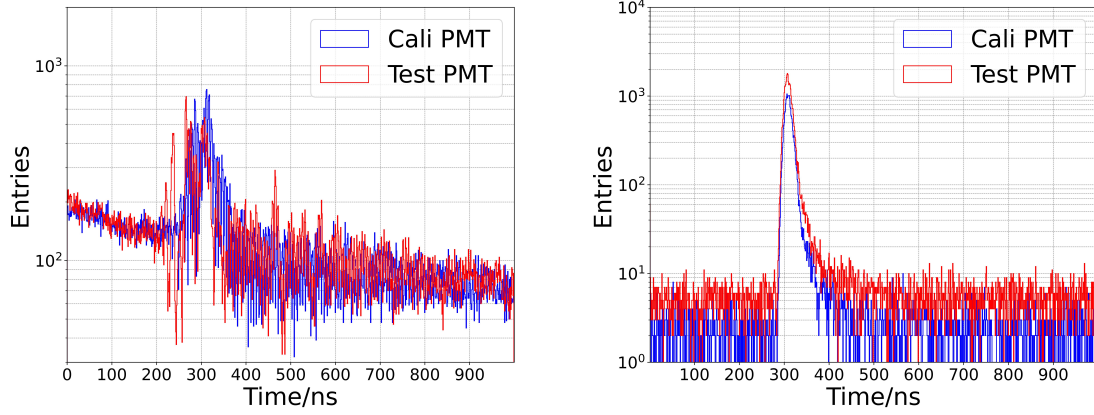


Fig 10 Time distribution of photoelectrons peaks from the calibration PMT and the test PMT before (left) and after (right) the pedestal cut. Blue (red) histogram represents the calibration (test) PMT. Data shown as an example come from a certain run.

4.2.2 Concentration factor

The number of non-zero hits N^{hit} is the total number of hits with the peak time position in the signal window with N^{total} observations. The DCR is estimated as the rate of the hits with the peak time position in the time window $[40 \text{ ns}, t_{\text{signal}} - 3\sigma_{\text{signal}}]$. The contribution from dark noise $N^{\text{noise}} = 6\sigma_{\text{signal}}N^{\text{total}} \times \text{DCR}$ is subtracted in the trigger ratio R as

$$R = (N^{\text{hit}} - N^{\text{noise}})/N^{\text{total}} \quad (1)$$

The number of photoelectrons in each observation obeys the Poisson distribution $\pi(\lambda)$, with the expected number λ as

$$\lambda = -\log(1 - R), \quad (2)$$

To eliminate the instability of the light source, we use the PE ratio $\eta \equiv \lambda_{\text{test}}/\lambda_{\text{calib}}$, where λ_{test} and λ_{calib} are λ s for the test and calibration PMTs, respectively. This ratio is independent of the intensity of the light source. The concentration factor $\eta^{\text{con}}/\eta^{\text{bare}}$ represents the boost in DE due to the concentrator, where η^{con} and η^{bare} are the PE ratio in the cases with and without the concentrator on the test PMT. The points in Fig. 11 show the measured angular responses of the concentration factors for four wavelengths at rail L1 and L2. The incident angle is defined as the angle between the vector from the center of the light concentrator to the center of the light source and the normal of the PMT.

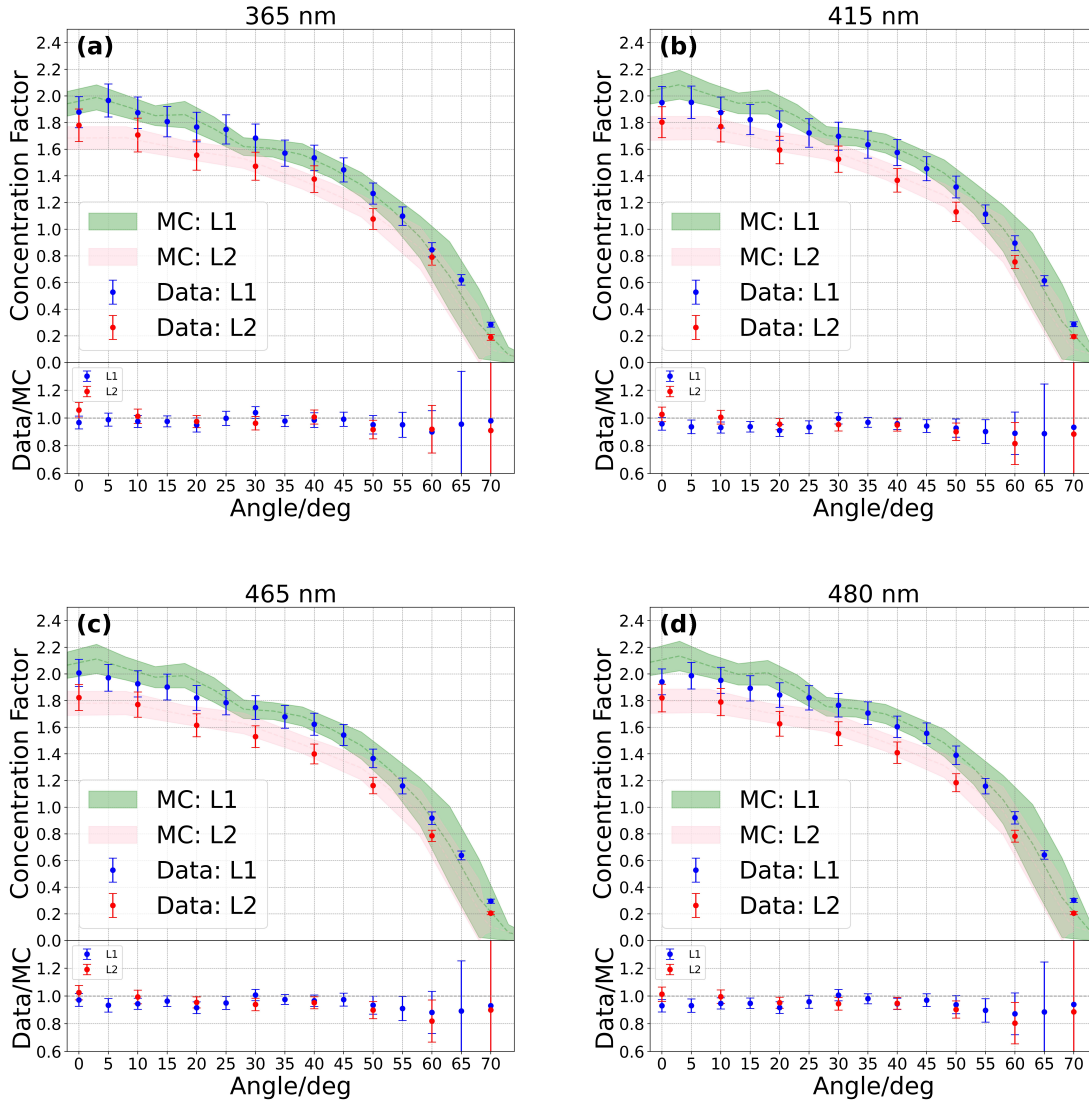


Fig 11 Angular responses of the concentration factors of data and MC for four wavelengths using the diffusion ball at rail L1 and L2. Top left (right) represents 365 (415) nm, and bottom left (right) represents 465 (480) nm. The ratio of data/MC panels show that the data and MC are in good agreement.

4.3 Monte Carlo simulations

Based on the geometry and physics of the PMT and the associated concentrator described in Sects. 2 and 3, we carried out a MC simulation to obtain the concentration factor. The simulation setup is the same as the experimental one, as shown in Fig. 8. The optical photons are isotropically emitted by a spherical source with diameter of 5 cm, and the measured reflectivity of the coated aluminum (shown in Fig. 7) is used as input for the simulation. For simplicity, we assume the absorptance of the dark box to be unity. The ratio η is calculated with the number of photons that hit the test and calibration PMTs and used to estimate the concentrator factor. The comparison of the concentrator factors between the simulation and the experiment can be found in Fig. 11. Good agreement is achieved between the simulation and the experiment.

We found that moving the light source around the rail can significantly affect the curve of the concentrator factor, especially if the incident angle is greater than 50° . In reality, the manufacturing artifact can bias the PMT's normal by a few degrees. By visual checking, the bias of $3 \pm 2^\circ$ is found and applied in the estimation of systematic uncertainty, i.e., the MC curve is shifted by $+3^\circ$ as the central line and further shifted by $\pm 2^\circ$ as the systematic uncertainty shown as the band in Fig. 11. The systematic uncertainties resulting from vertical and radial shifts of the light source by ± 1 cm are also studied. In the incident angle range $0 - 50^\circ$, these three systematic errors are similar with a value less than 5%, while the angular uncertainty becomes dominant beyond 50° .

4.4 Systematic uncertainty

Two systematic uncertainties for the experimental measurement are considered, which are summarized in Table 3. In the measurement, we used the diffusion ball of different diameters of 2.0, 3.0, 4.0, and 5.0 cm, respectively. To be conservative, we assign the maximum difference between the mean and the largest/smallest of the measured concentrator factors as the systematic uncertainty, which is less than 6.1% for the four wavelengths. The second uncertainty arises from the installation of the light concentrator. For each wavelength, we measured the concentrator factor in five installation sets using the case of the 5.0 cm diffusion ball and the incident angle of 0° as the base. The method for estimating the installation uncertainty is the same as that for the diameter.

Table 3 Summary of systematic uncertainties for the experimental measurement. The second and third columns list the uncertainty from the diameter of the diffusion ball and the installation of the light concentrator, and the fourth one is the total systematic uncertainty which is the quadratic sum of the second and third columns.

Wavelength (nm)	Diameter	Installation	Total
365	3.8%	4.9%	6.2%
415	6.1%	1.0%	6.2%
465	4.9%	1.2%	5.1%
480	4.9%	0.8%	5.0%

5 Discussion

5.1 Low background

The JNE experiment aims to detect rare neutrino signals in the deep laboratory. To minimize interference from other background radiation as much as possible, we should use low-radioactivity background materials to construct the detector, including the stainless steel, acrylic, ropes, and PMTs. Currently, the mass of one concentrator is approximately 4 kg, about 12 tons of ABS plastic are needed to make all the concentrators. When choosing ABS materials, it is necessary to ensure the high cleanliness of the raw materials and processing procedures to minimize the impact of the radioactive background of ABS plastic on neutrino detection.

5.2 The protection of aluminum film

During the trial and testing process of the concentrator sample, the aluminum film used did not have a protective coating. Considering that the concentrator will be stored in air, installed, and used in pure water in the future, it is difficult to guarantee the stability of the naked aluminum film. For instance, oxidation reactions can cause the aluminum film to turn black, reducing its

reflectivity. To ensure the long-term stability and optical performance of the aluminum film, we refer to the method of the SNO experiment and propose to apply a protective layer to the aluminum film. Although the introduction of the protective layer may have a certain impact on the reflectivity of the aluminum film, by choosing the appropriate material and designing a reasonable coating thickness, this impact can be minimized.

5.3 Improvement of light collection efficiency and energy resolution

MC simulations using a parallel light source instead of the diffusion ball are performed with other conditions unchanged to eliminate the geometric effect. The angular responses of the concentrator factors, in this case, are shown in Fig. 12. Note that here the concentrator factor is defined as the ratio of the number of photons that hit the region of the exit aperture with the concentrator to that without it, i.e. the area below the mask is not accounted for. By this definition, the contribution of a more significant TTS part around the equator of PMT, as shown in the right panel of Fig. 3, is eliminated. The curve of the concentrator factor moves upward as the wavelength increases due to the higher reflectivity. We expect an improvement in energy resolution by more than 15% for events in the center of the JNE detector.

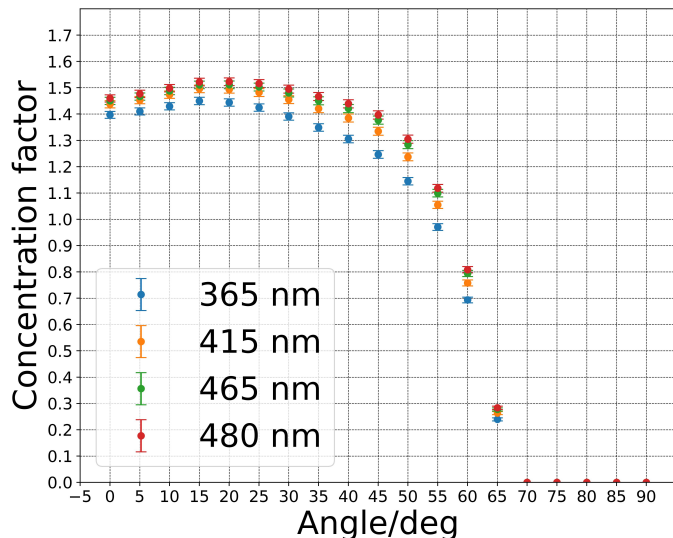


Fig 12 Angular responses of the concentration factors for four wavelengths using the simulated parallel light.

6 Conclusion

A custom-designed light concentrator is developed to match the NNVT 8-inch MCP-PMT of the JNE. With the combination of PMT and light concentrator, it is expected that the energy resolution will improve by more than 15% for events at the center of the JNE detector, while the TTS will only increase by no more than 0.3 ns (FWHM). Furthermore, the combined structure has long-term stability, making it suitable for the JNE detector’s photoelectron-detecting device.

Acknowledgments

This work is supported in part by the Discipline Construction Fund of Shandong University, the Key Laboratory of Particle & Radiation Imaging (Tsinghua University), and the CAS Center for Excellence in Particle Physics (CCEPP), the National Natural Science Foundation of China (Nos. 12127808, 12141503, and 11620101004), the China Postdoctoral Science Foundation (Certificate Number: 2024M751611), and the Ministry of Science and Technology of China (No. 2022YFA1604704). We thank the State Key Laboratory of New Ceramics & Fine Processing of Tsinghua University for measuring the reflectivity of coated aluminum. The authors acknowledge Orrin Science Technology and Jingyifan Co., Ltd for the efforts in the engineering design and fabrication of the dark box.

References

- 1 J. F. Beacom *et al.*, “Physics prospects of the Jinping neutrino experiment,” *Chin. Phys. C* **41**(2), 023002 (2017).
- 2 H. Ma, W. Dai, Z. Zeng, *et al.*, “Status and prospect of China Jinping Underground Laboratory,” *J. Phys. Conf. Ser.* **2156**(1), 012170 (2021).
- 3 Y. Fukuda *et al.*, “The Super-Kamiokande detector,” *Nucl. Instrum. Meth. A* **501**, 418–462 (2003).
- 4 J. Boger *et al.*, “The Sudbury neutrino observatory,” *Nucl. Instrum. Meth. A* **449**, 172–207 (2000).
- 5 F. P. An *et al.*, “Observation of electron-antineutrino disappearance at Daya Bay,” *Phys. Rev. Lett.* **108**, 171803 (2012).
- 6 G. Alimonti *et al.*, “The Borexino detector at the Laboratori Nazionali del Gran Sasso,” *Nucl. Instrum. Meth. A* **600**, 568–593 (2009).
- 7 M. G. Aartsen *et al.*, “The IceCube Neutrino Observatory: Instrumentation and Online Systems,” *JINST* **12**(03), P03012 (2017). [Erratum: *JINST* **19**, E05001 (2024)].
- 8 X.-J. Xu, Z. Wang, and S. Chen, “Solar neutrino physics,” *Prog. Part. Nucl. Phys.* **131**, 104043 (2023).
- 9 G. Bellini, A. Ianni, L. Ludhova, *et al.*, “Geo-neutrinos,” *Prog. Part. Nucl. Phys.* **73**, 1–34 (2013).
- 10 A. De Gouvêa, I. Martinez-Soler, Y. F. Perez-Gonzalez, *et al.*, “Fundamental physics with the diffuse supernova background neutrinos,” *Phys. Rev. D* **102**, 123012 (2020).
- 11 M. J. Dolinski, A. W. P. Poon, and W. Rodejohann, “Neutrinoless Double-Beta Decay: Status and Prospects,” *Ann. Rev. Nucl. Part. Sci.* **69**, 219–251 (2019).
- 12 Z. Wang, Y. Liu, S. Chen, *et al.*, “Structural design of the acrylic vessel for the Jinping Neutrino Experiment,” *JINST* **19**(07), P07041 (2024).
- 13 Z. Guo, M. Yeh, R. Zhang, *et al.*, “Slow Liquid Scintillator Candidates for MeV-scale Neutrino Experiments,” *Astropart. Phys.* **109**, 33–40 (2019).
- 14 W. Shao, W. Xu, Y. Liang, *et al.*, “The potential to probe solar neutrino physics with LiCl water solution,” *Eur. Phys. J. C* **83**(9), 799 (2023).
- 15 A. Zhang, B. Xu, J. Weng, *et al.*, “Performance evaluation of the 8-inch MCP-PMT for Jinping Neutrino Experiment,” *Nucl. Instrum. Meth. A* **1055**, 168506 (2023).

- 16 M. D. Lay and M. J. Lyon, “An experimental and Monte Carlo investigation of the R1408 Hamamatsu 8-inch photomultiplier tube and associated concentrator to be used in the Sudbury Neutrino Observatory,” *Nucl. Instrum. Meth. A* **383**, 495–505 (1996).
- 17 A. Allega *et al.*, “Evidence of Antineutrinos from Distant Reactors using Pure Water at SNO+,” *Phys. Rev. Lett.* **130**(9), 091801 (2023).
- 18 L. Oberauer, C. Grieb, F. von Feilitzsch, *et al.*, “Light concentrators for Borexino and CTF,” *Nucl. Instrum. Meth. A* **530**, 453–462 (2004).
- 19 K. Loo, “Upgrade of OSIRIS for Future Liquid Scintillator Studies,” *PoS TAUP2023*, 319 (2024).
- 20 J. A. Aguilar, A. Basili, V. Boccone, *et al.*, “Design, optimization and characterization of the light concentrators of the single-mirror small size telescopes of the Cherenkov Telescope Array,” *Astropart. Phys.* **60**, 32–40 (2015).
- 21 P. Krizan, “Novel photon detectors,” *Nucl. Instrum. Meth. A* **1065**, 169482 (2024).
- 22 Y. Zhi, Y. Liang, Z. Wang, *et al.*, “Wide field-of-view and high-efficiency light concentrator,” *Nucl. Instrum. Meth. A* **885**, 114–118 (2018).
- 23 J. Weng, A. Zhang, Q. Wu, *et al.*, “Single electron charge spectra of 8-inch high-collection-efficiency MCP-PMTs,” *Nucl. Instrum. Meth. A* **1066**, 169626 (2024).
- 24 ASTM International, *Standard test method for tensile properties of plastics* (2014).
- 25 Altair Engineering Inc. Available online: <https://altair.com/altair-hyperworks>.
- 26 H. D. Hibbitt, “ABAQUS/EPGEN—A general purpose finite element code with emphasis on nonlinear applications,” *Nuclear Engineering and Design* **77**(3), 271–297 (1984).
- 27 H. Yang, T. Xue, L. Jiang, *et al.*, “Quantitative analysis of the high speed and high precision waveform digital system for Jinping Neutrino Experiment,” *JINST* **19**(08), T08005 (2024).